Geophysical Prospecting

EAGE EUROPEAN ASSOCIATION OF GEOSCIENTISTS & ENGINEERS

Geophysical Prospecting, 2016, **64**, 83–101 doi: 10.1111/1365-2478.12253

Inversion of multicomponent seismic time shifts for reservoir pressure and length: a feasibility study

Steven Shawn Smith[1*,†] and Ilya Tsvankin[2]

[1]*Shell Westhollow Technology Center, Houston, TX 77077, USA, and* [2]*Center for Wave Phenomena (CWP), Department of Geophysics, Colorado School of Mines (CSM), Golden, CO 80401, USA*

Received September 2013, revision accepted January 2015

ABSTRACT

Pressure drops associated with reservoir production generate excess stress and strain that cause travel-time shifts of reflected waves. Here, we invert time shifts of P-, S-, and PS-waves measured between baseline and monitor surveys for pressure reduction and reservoir length. The inversion results can be used to estimate compaction-induced stress and strain changes around the reservoir. We implement a hybrid inversion algorithm that incorporates elements of gradient, global/genetic, and nearest neighbour methods and permits exploration of the parameter space while simultaneously following local misfit gradients. Our synthetic examples indicate that optimal estimates of reservoir pressure from P-wave data can be obtained using the reflections from the reservoir top. For S-waves, time shifts from the top of the reservoir can be accurately inverted for pressure if the noise level is low. However, if noise contamination is significant, it is preferable to use S-wave data (or combined shifts of all three modes) from reflectors beneath the reservoir. Joint wave type inversions demonstrate improvements over any single pure mode. Reservoir length can be estimated using the time shifts of any mode from the reservoir top or deeper reflectors. We also evaluate the differences between the actual strain field and those corresponding to the best-case inversion results obtained using P- and S-wave data. Another series of tests addresses the inversion of the time shifts for the pressure drops in two-compartment reservoirs, as well as for the associated strain field. Numerical testing shows that a potentially serious source of error in the inversion is a distortion in the strain-sensitivity coefficients, which govern the magnitude of stiffness changes. This feasibility study suggests which wave types and reflector locations may provide the most accurate estimates of reservoir parameters from compaction-induced time shifts.

Key words: Geomechanics, Seismic modelling, Inversion, Stress-induced anisotropy, Converted waves, Shear waves, Time lapse, Compacting reservoir, Transverse isotropy, VTI.

INTRODUCTION

Pressure variations inside a petroleum reservoir influence drilling and production decisions throughout the life of the field. Inversion for the pressure distribution in multicompartment reservoir models permits identification of depleted zones and isolated compartments sealed off by geologic formations (Greaves and Fulp 1987; Landrø 2001; Lumley 2001; Calvert

*E-mail: SteveSmithCSM@aol.com
†Formerly at: Center for Wave Phenomena (CWP), Department of Geophysics, Colorado School of Mines (CSM), Golden, CO 80401 USA

© 2015 European Association of Geoscientists & Engineers

2005; Hodgson *et al.* 2007; Wikel 2008). Pressure inversion may also identify regions of elevated stress and strain where existing wells may fail, or additional drilling should be avoided.

Most existing publications on modelling and estimation of production-induced strains and time shifts have relied on vertical-strain formulations (Hatchell and Bourne 2005; Janssen, Smith, and Byerley 2006; Roste 2007; Hodgson *et al.* 2007; Staples *et al.* 2007; De Gennaro *et al.* 2008). MacBeth (2004) describes pressure-dependent variation of sandstone bulk and shear moduli as a function of empirically determined vertical and tangential compliance coefficients. MacBeth, Floricich, and Soldo (2006) demonstrate agreement between 4D reservoir characteristics estimated from field data and those obtained from models employing directionally-dependent rock physics and AVO-based coefficients that scale oil saturation and pressure variations. However, several studies have shown that modelling of triaxial strains/stresses is necessary because shear strains significantly contribute to stiffness perturbations and, thus, time shifts (Schutjens *et al.* 2004; Sayers and Schutjens 2007; Herwanger 2008; Fuck, Bakulin, and Tsvankin 2009; Sayers 2010; Fuck, Tsvankin, and Bakulin 2011; Smith and Tsvankin 2012).

Time shifts and, ultimately, reservoir pressure estimated from seismic data can be highly dependent on processing methods, the geomechanical model, and the quality of the recorded waveforms. A process known as "cross-equalization" (Rickett and Lumley 1998; 2001) is typically applied to field data for the purpose of making them suitable for time-lapse inversion. Time-shift computation from synthetic data still requires post-processing of the modelled reflected wavefields designed to suppress artefacts caused by interfering arrivals (Smith and Tsvankin 2012).

Using geomechanical modelling and time-shift analysis, Fuck *et al.* (2009) demonstrate that it is essential to account for triaxial stress and stress-induced anisotropy in describing offset-dependent P-wave time shifts. Smith and Tsvankin (2012) extend time-shift modelling to multicomponent data and study the variation of P-, S-, and PS-wave time shifts with reservoir pressure and reflector depth (here, by S-waves, we mean the SV-mode). Because stress-induced anisotropy is close to elliptical, the velocity of SV-waves and of the SV-leg of PS-waves is almost independent of direction. Large compaction-induced strains inside the reservoir generate S-wave time shifts for deep reflectors that are two to three times larger than those for P-waves. A sensitivity study by Smith and Tsvankin (2013) demonstrates that S-wave time shifts for reflectors beneath the reservoir become nonlinear in pressure for relatively large stiffness changes corresponding to pressure reductions exceeding approximately 10%. Their results suggest that time shifts of shear-wave reflections may be large enough to invert for reservoir pressure when the smaller P-wave shifts are obfuscated by noise.

Here, we present integrated 2D geomechanical/seismic inversion of compaction-induced time shifts obtained from multicomponent seismic data generated for single- and two-compartment reservoir models. The reservoir is embedded in a homogeneous isotropic background medium that becomes heterogeneous and anisotropic after the pressure reduction. The time shifts are estimated using P-, S-, and PS-wave reflections from three interfaces around the reservoir. Our inversion algorithm combines global and gradient techniques with the goal of both exploring the model space and ensuring convergence toward a global minimum. Inversion for reservoir pressure and length is performed for each mode (P, S, and PS) separately, as well as for the combination of time shifts of all three wave types. We also examine the differences between the strain field of the reference reservoir and those of the best inverted models. Finally, we investigate the ability of reflection data to resolve the pressure differences and strain-field perturbations for a two-compartment reservoir.

THEORETICAL BACKGROUND

Geomechanical and time-shift modelling

Various far-field stress/strain relationships have been published for an inclusion undergoing thermal or pressure changes (McCann and Wilts 1951; Mindlin and Cheng 1950; Geertsma 1973; Hu 1989; Downs and Faux 1995). In what has become a standard method, Hodgson *et al.* (2007) invert time shifts for the vertical strain ϵ_{zz} due to a superposition of such inclusions using the "*R*-factor" equation of Hatchell and Bourne (2005):

$$\frac{\Delta t}{t} = (1 + R)\,\epsilon_{zz}, \tag{1}$$

where Δt is the estimated P-wave traveltime shift, t is the P-wave traveltime, and R is a coefficient empirically determined from field-survey time-shift measurements. Then pressure reductions can be estimated from ϵ_{zz} by incrementally updating rock physics and geologic properties with the help of well logs and seismic data. However, rocks both inside and outside a producing reservoir are subject to spatially and temporally varying combinations of vertical and horizontal stresses (e.g., Herwanger 2008), indicating the need to account for triaxial stress/strain.

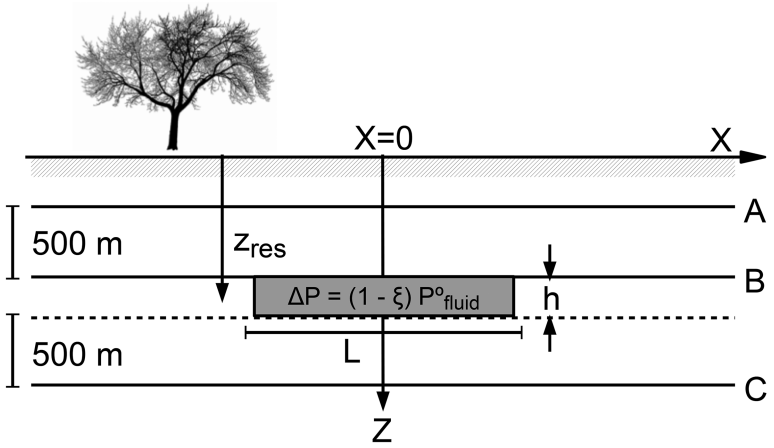

Figure 1 Compacting reservoir and reflectors (marked A, B, and C) used to measure travel-time shifts. ΔP is the change in the initial reservoir fluid pressure [see equation (2)]. The reservoir is at a depth of 1.5 km and measures 2.1 km in length (L) and 0.1 km in thickness (h). The unstressed reservoir and surrounding medium are homogeneous with density $\rho = 2140\,\mathrm{kg/m^3}$, velocities $V_P = 2300$ m/s, and $V_S = 1640$ m/s, and the third-order stiffness coefficients $C_{111} = -13,904$ GPa, $C_{112} = 533$ GPa, and $C_{155} = 481$ GPa (Sarkar *et al.* 2003).

Here, we invert for reservoir pressure and length using time shifts estimated from coupled geomechanical and seismic modelling (Smith and Tsvankin 2012). The strain field around the compacting reservoir in Fig. 1 is computed with triaxial plane-strain finite-element modelling (COMSOL AB 2008). The section is composed of a homogeneous unstressed material, and the effective pressure in the region designated as the reservoir is given by:

$$P_{\mathrm{eff}} = P_{\mathrm{c}} - \alpha P_{\mathrm{fluid}} = P_{\mathrm{c}} - \alpha\left(\xi P^{\circ}_{\mathrm{fluid}}\right), \tag{2}$$

where P_{c} is the confining pressure of the overburden column, P_{fluid} is the pressure of the fluid in the pore space, and $P^{\circ}_{\mathrm{fluid}}$ is the initial fluid pressure. Parameter α is an effective stress coefficient describing the response of the aggregate fluid and rock matrix, and ξ is responsible for scaling reservoir fluid pressure (depressurization). Thus, the reservoir pressure drop is $\Delta P = \Delta P_{\mathrm{fluid}} = (1 - \xi) P^{\circ}_{\mathrm{fluid}}$. Effective stress reductions, oriented normal to the boundaries of the reservoir volume (Fig. 1), are used in the finite-element software to compute the complete strain tensor. Variations in reservoir shape or orientation (geologic structure) may perturb the near-field strain and resulting time shifts of reflected waves (Smith and Tsvankin 2012).

Strain-induced changes in the second-order stiffness values c_{ijkl}, which serve as input to seismic modelling, are computed using the so-called nonlinear theory of elasticity (Hearmon 1953; Thurston and Brugger 1964; Fuck *et al.* 2009):

$$c_{ijkl} = c^{\circ}_{ijkl} + \frac{\partial c_{ijkl}}{\partial e_{mn}} \Delta e_{mn} = c^{o}_{ijkl} + c_{ijklmn}\, \Delta e_{mn}, \tag{3}$$

where c^{o}_{ijkl} is the stiffness tensor of the background (unperturbed) medium, c_{ijklmn} is the sixth-order "strain-sensitivity" tensor, and Δe_{mn} is the excess strain tensor. Index pairs of the tensor c_{ijklmn} can be contracted into single indices changing from 1 to 6 using Voigt notation (e.g., Tsvankin 2005), which results in the strain-sensitivity matrix $C_{\alpha\beta\gamma}$. If the background medium is isotropic (as assumed here), only C_{111} and C_{112} are necessary for computing time shifts caused by both volumetric (compressional) and deviatoric (shear) strains (Fuck *et al.* 2009).

Pore-pressure ($P_{\mathrm{p}} = P_{\mathrm{fluid}}$) reduction within the 2D reservoir block (Fig. 1) produces a strain field that results in a transversely isotropic medium with a tilted axis of symmetry (TTI) (Tsvankin 2005; Fuck *et al.* 2011). Coefficient α can change with reservoir properties, making equation (2) nonlinear in pressure for large compaction/porosity changes. However, for the range of effective pressures in this study, α is approximately constant (Hornby 1996). The depressurization and fluid type of each reservoir compartment are assumed to be uniform. Further, we do not consider large bulk moduli changes, which can occur when gas escapes from pore fluids (i.e., pressure drops below the "bubble point") (Batzle and Han 2009), or the replacement of oil by water.

We employ a 2D elastic anisotropic finite-difference code (Sava, Yan, and Godwin 2010) to generate multicomponent P-, S-, and PS-wave data for the baseline ($\Delta P = 0$) and monitor ($\Delta P > 0$) surveys. Reflectors measuring one grid point in thickness are inserted into the model as density anomalies. Using baseline/monitor cross-correlations on shot gather data, time shifts for P-waves are estimated using the vertical (Z) displacement component, whereas those for S(SV)- and PS-wave data are estimated on the horizontal (X) component. The modelled time shifts for P-, S-, and PS-waves are then fit with polynomials to produce smooth curves as a function of the lateral coordinate at reflectors A, B, and C (Fig. 1). Similar post-processing, including resampling, filtering, stacking,

amplitude matching, etc. (referred to as cross-equalization), is typically applied to field data prior to time-shift estimation (Rickett and Lumley 1998; 2001; Magnesan *et al.* 2005).

INVERSION METHODOLOGY

Properties of multicomponent time shifts

Time shifts are estimated from synthetic data generated for the depressurized reference reservoir in Fig. 1. Figure 2 shows time shifts of reflected P-, S-, and PS-waves for a fluid-pressure drop of 20% with the source located above the reservoir centre. The spatial patterns of compaction-induced time shifts remain consistent over a range of pressure drops, and reflectors A, B, and C are positioned to sample these distributions for inversion purposes. Compaction-induced strains in the reservoir volume are one-to-two orders of magnitude larger than those in the surrounding medium (Smith and Tsvankin 2013). The resulting velocity increase inside the reservoir causes time shifts to change from lags in the overburden to leads beneath the reservoir. Therefore, the reservoir essentially behaves like a high-velocity lens for all wave types.

P-wave time shifts (Fig. 2a) exhibit pronounced offset variations around the reservoir due to the stress-induced anisotropy. While SV-wave anisotropy is weak, shear-wave time shifts from reflection points beneath the reservoir are two to three times larger than those of P-waves (Fig. 2b). PS-wave time-shift trends (Fig. 2c) depend on the reflection (conversion) point, and for reflectors beneath the reservoir, they are governed by the combination of P-wave lags in the overburden and larger S-wave leads accumulated inside the reservoir. For reflectors in the overburden, S-wave leads practically cancel P-wave lags, and time shifts of PS-waves are generally small (Smith and Tsvankin 2012). Variations in these time-shift patterns occur with source location and the proximity of the reservoir to the free surface.

Multicompartment reservoirs exhibit time-shift distributions similar to those in Fig. 2 but with strain and time-shift perturbations caused by the intercompartment pressure differences or variations in shape (Smith and Tsvankin 2012, 2013). The results for a single-compartment reservoir presented here highlight the general properties of time shifts of different wave types for a wide range of reflector depths. Complicating the model by introducing a multicompartment reservoir (below) or a heterogeneous background reduces the degree of generality, making the results specific to a certain geologic section.

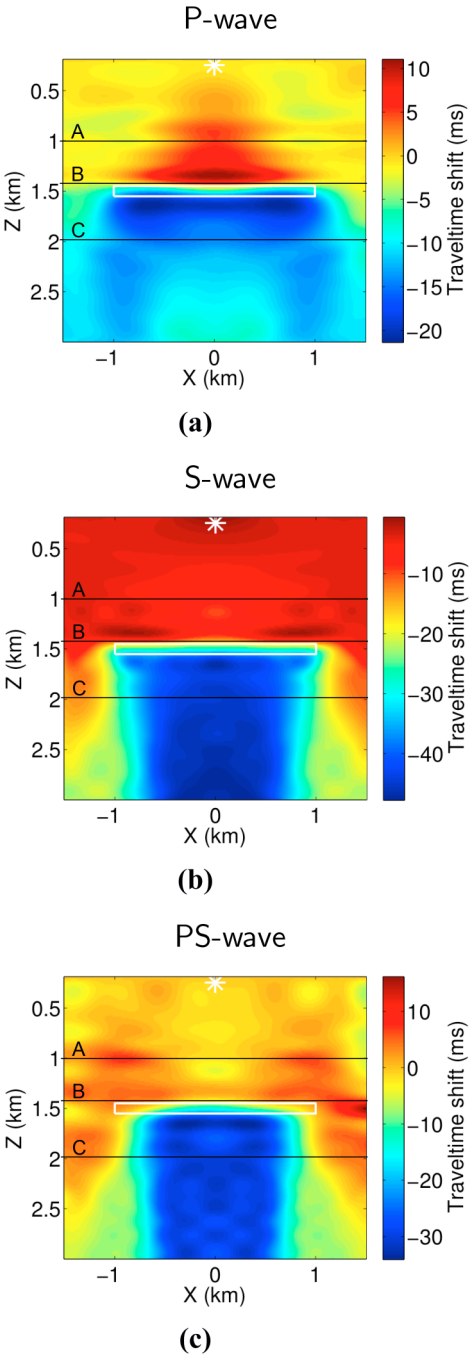

Figure 2 Typical two-way time-shift distributions for (a) P-waves, (b) S-waves, and (c) PS-waves measured using 22 reflectors around the reservoir (white box) from Fig. 1 (Smith and Tsvankin 2013). The time shifts correspond to hypothetical specular reflection points at each (*X*, *Z*) location in the subsurface; source location is indicated by the white asterisk at the top. Positive shifts indicate lags where monitor survey reflections arrive later than the baseline events; negative shifts are leads.

Model properties and inversion constraints

As in our previous publications, the single-compartment reservoir is composed of and embedded in a homogeneous material with the properties of Berea sandstone (Fig. 1). The effective stress coefficient α for the reservoir is 0.85 [equation (2)]. Velocities are reduced by 10% from the laboratory values to account for the difference between static and dynamic stiffness values in low-porosity rocks (Yale and Jamieson 1994). The two-compartment reservoir introduced below is simply the existing reservoir divided in half to form two equally sized sections.

For geomechanical modelling, the reservoir is located in a finite-element mesh measuring 20 km × 10 km, which allows us to obtain stress, strain, and displacement close to those for a half-space. The pressure reduction in the reference (actual) reservoir is 17.5%, with pressure drops of the inversion models constrained to be between 10% and 20% ($0.8P^{\circ}_{\text{fluid}} \leq P_{\text{fluid}} \leq 0.9P^{\circ}_{\text{fluid}}$, with the actual value $0.825P^{\circ}_{\text{fluid}}$). The reservoir length is varied between 1.5 km and 2.5 km; the actual value $L = 2.1$ km. Such ranges are not unrealistic because the reservoir pressure and length typically can be estimated from well pressure at depth and seismic images, respectively. Due to the high computational cost of forward modelling and post-processing, it is currently impractical for us to run inversions for a wider range of these parameters.

Objective function

Both the reference reservoir and trial inversion models are depressurized from an initial zero-stress/strain state. Misfits (objective functions) for P-, S-, and PS-wave time shifts Δt for trial reservoir models are computed as the L2-norm,

$$\mu = \sqrt{\sum_{k=1}^{N} \left(\Delta t_k^{\text{ref}} - \Delta t_k\right)^2}, \tag{4}$$

where Δt^{ref} are the time shifts for the reference reservoir, and $k = 1, 2, ..., N$ are the individual traces in the shot record. For both the baseline and monitor surveys, we use a single source located above the centre of the reservoir (Fig. 2). Time-shift trends for sources displaced with respect to the reservoir centre are discussed in Smith and Tsvankin (2012). In principle, the methodology employed here can be implemented for multiple shot records and reflector/wave-type combinations.

The joint misfit for all three wave types (P, S, and PS) is the L2-norm of the individual wave-type misfits,

$$\mu_{\text{joint}} = \sqrt{\mu_{\text{P}}^2 + \mu_{\text{S}}^2 + \mu_{\text{PS}}^2}. \tag{5}$$

Misfits discussed below have not been normalized to facilitate comparison of results for different wave types at specific reflectors. As aforementioned, the smoothing of time shifts in post-processing amounts to an unspecified regularization term added to equation (4).

To evaluate the stability of the inversion algorithm, time shifts for the reference reservoir are contaminated by Gaussian noise with standard deviations of 5 ms and 10 ms (we also present results for noise-free data). This noise corresponds to moderate (5 ms) and significant (10 ms) levels of time-shift errors with respect to the P-wave shifts in Fig. 2a. Although average noise of 10 ms may be comparable to P-wave time shifts measured in the field, it amounts to about 50% of the P-wave shifts directly beneath the reservoir and only 25% of the S-wave shifts below the reservoir. While low levels of noise can mask and smooth out only short-length features in the time-shift curves, higher noise can distort time-shift behaviour at all scales. The influence of noise on misfit characteristics is discussed in Appendix B.

Inversion algorithm

Here we invert for reservoir pressure drop (ΔP) and length (L). Potentially, it may be possible to simultaneously estimate other reservoir parameters (e.g., the elastic properties and effective stress coefficient) or the pressure distribution in multiple (more than two) compartments. In fact, the methods described here can be applied to more complicated reservoir geometries by further compartmentalizing the reservoir.

Changes in time shifts with respect to pressure-induced stiffness perturbations are generally nonlinear (Smith and Tsvankin 2013). Time shifts become increasingly nonlinear for shorter reservoirs with large stress/strain anomalies at the corners. Therefore, we have devised a hybrid inversion technique (Appendix A) that combines the convergence characteristics of a gradient algorithm with the ability of global inversion to identify and avoid local minima.

Our method is based on the "nearest neighbour" algorithm of Sambridge (1999) that samples the parameter space, dividing it into so-called Voronoi cells. The nearest neighbour technique selects a subset of minimum-misfit models to update, and it further divides those cells by inserting new models via a random walk or a Gibbs sampler within the cell. This procedure helps obtain a discrete (compartmentalized)

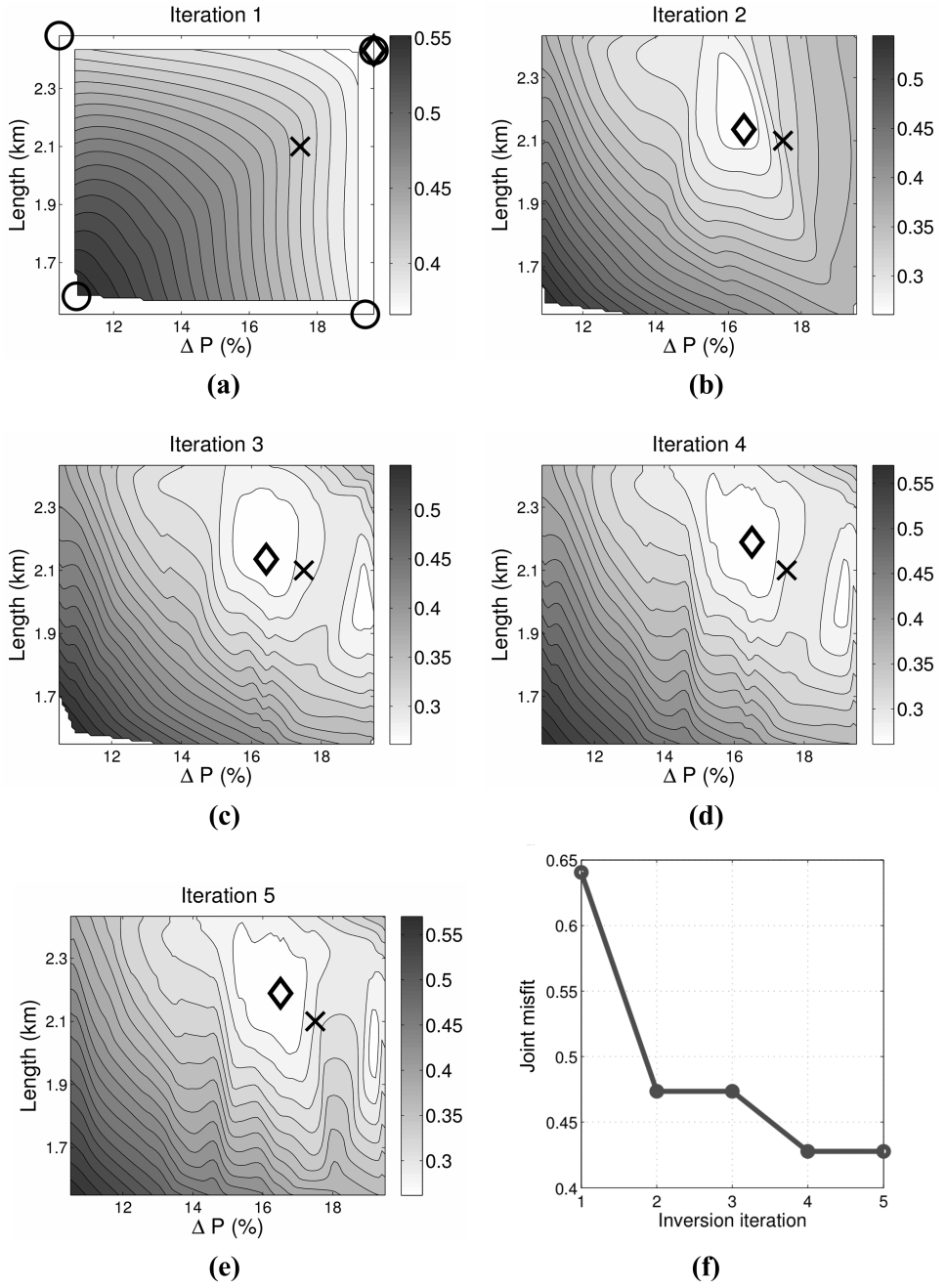

Figure 3 Evolution of misfit surfaces for the inversion of joint-misfit data [equation (5)] from reflector C. Plot (a) shows the locations of the initial inversion models (circles). Five iterations (a-e) were completed, employing 57 forward models. The normalized minimum joint misfit (f) falls by approximately 25%, and the sub-tolerance change in misfit between iterations 4 and 5 terminated the inversion. Reference reservoir time shifts were contaminated with Gaussian noise having a standard deviation of 5 ms. The surfaces are interpolated between the misfit values for all models computed through the specified iteration. The reference reservoir pressure drop and length (marked by the cross) are 17.5% and 2.1 km, respectively. The location of the minimum-misfit model at each iteration is marked by a diamond, with a final solution (plot e) of $\Delta P = 16.5\%$ and $L = 2.19$ km.

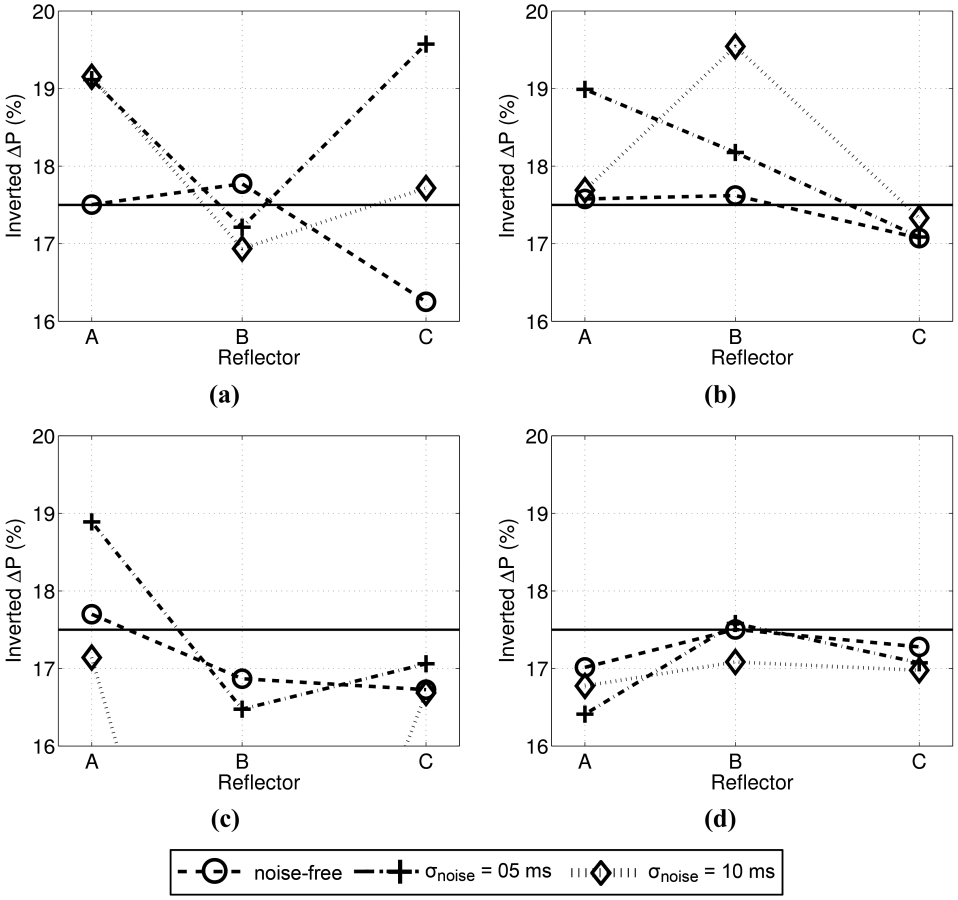

Figure 4 Inverted reservoir pressure drop using time-shift misfits of (a) P-waves, (b) S-waves, (c) PS-waves, and (d) the combination of all three modes (joint misfits). The actual reservoir pressure drop (marked by solid line) is 17.5%. Plot legends indicate the standard deviation of Gaussian noise added to the time shifts of the reference reservoir. The inverted $\Delta P = 10.4\%$ for PS-waves from reflector B with $\sigma_{\text{noise}} = 10$ ms is located outside the plot.

estimate of the misfit, but it does not give any gradient information. Thus, model updates may be located up-gradient from local or global minima, reducing the rate of convergence. To better update the existing set of inversion models, our algorithm estimates the local gradient using some of the minimum-misfit models. The global portion of the algorithm is designed to fill unsampled voids in the parameter space, preventing the search from getting trapped in local minima. Due to the method's simple implementation, multiple gradient trackers can simultaneously converge toward local minima or, if found, the global minimum.

Evolution of the misfit surface

Figure 3a–e demonstrates the ability of the algorithm to reconstruct the structure of the misfit surface (2D slice in multiparameter inversions) for noise-contaminated data while converging to local/global minima. Figure 3f shows how the objective function that includes misfits of all three modes [equation (5)] from reflector C changes during five inversion iterations.

Four initial models (black circles in Fig. 3a) were placed in the parameter space using a pseudo-regular distribution, which ensures that they are not equidistant from one another. Thus, the step sizes of the initial-model updates are different, and the parameter space is well sampled prior to the next iteration. At each iteration, a single minimum-misfit model was used for gradient estimation and model updates (see Appendix A). In addition to updated models inserted near the current low-misfit models, ten "exploration" models per iteration were added to better sample the parameter space. The maximum number of computed models was set to 100.

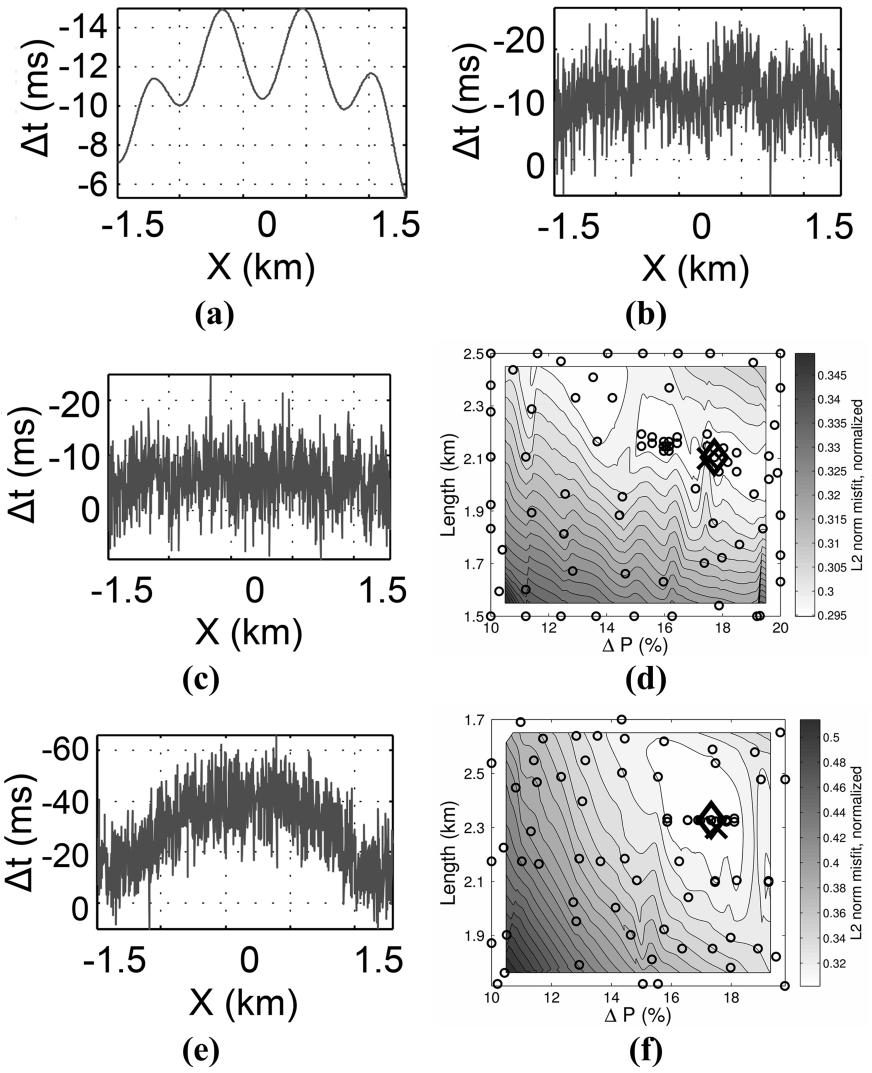

Figure 5 Computed P-wave time shifts versus offset $[\Delta t(x)]$ from reflector C for (a) noise-free data (Fig. 2a), (b) $\sigma_{\text{noise}} = 5$ ms, and (c) $\sigma_{\text{noise}} = 10$ ms. (d) The misfit surface for P-waves from reflector C with $\sigma_{\text{noise}} = 10$ ms; the actual parameters are marked by the cross, and inverted parameters are marked by the diamond. Circles indicate models used in the inversion. (e) S-wave time shifts from reflector C with $\sigma_{\text{noise}} = 10$ ms (Fig. 2b), and (f) the misfit surface for the S-wave shifts from plot (e).

By the third iteration (Fig. 3c), the general structure of the misfit surface is reasonably well defined by the exploration models. The normalized joint misfit drops by approximately 25% in only five iterations (Fig. 3f), resulting in an inverted pressure drop of 16.5% and reservoir length of 2.19 km (both are reasonably close to the actual values). Increasing the number of minimum-misfit/gradient-estimation models will further reduce the minimum-misfit and improve the rate of convergence. Additional misfit reductions can be achieved by adjusting the termination conditions (Appendix A).

ANALYSIS OF NUMERICAL RESULTS

For the entire set of inversion results, the reference reservoir parameters and constraints on the unknowns are the same as those in Fig. 3. While only one minimum-misfit model was used for gradient tracking in Fig. 3, two gradient trackers were employed in all of the examples discussed below to increase convergence rates and resolve multiple minima. The maximum number of allowed forward models was also increased from 100 to 200. A minimum of 80 forward models and three iterations were required before tolerance-based termination was permitted.

Inverted pressure and length

All pressure-inversion results arranged by wave type are displayed in Fig. 4. Because P-wave time shifts in the overburden are small (Fig. 2a), they are easily masked by noise. Thus, P-wave inversion for reflector A is successful only for noise-free data (Fig. 4a). However, the magnitude of the P-wave shifts accumulated in the overburden increases with depth and reaches maximum values at the reservoir top (reflector B). Further, these elevated P-wave shifts extend laterally across the entire reservoir (Fig. 2a). Consequently, inversion of P-wave shifts for reflector B yields accurate pressure estimates even for 10-ms noise. P-wave time-shift magnitudes are largest immediately beneath the reservoir due to elevated strains inside it (Fig. 2a; see Smith and Tsvankin 2013) but decrease to 10–15 ms at reflector C (Fig. 5a). Thus, the higher frequency time-shift trend of the noise-free data from reflector C (Fig. 5a) remains somewhat visible in the time shifts for $\sigma_{\text{noise}} = 5$ ms (Fig. 5b), particularly on the right-hand side of the measurements. This pattern, however, is severely distorted by 10-ms noise (Fig. 5c), which results in a large null space in the inversion for ΔP and L (Fig. 5d; see Appendix B).

Therefore, the accurate pressure estimate obtained for the P-wave data from reflector C with $\sigma_{\text{noise}} = 10$ ms is likely due to the algorithm's ability to locate a narrow minimum on the misfit surface. Similar to signal pre-whitening for optimal time-domain filter design, the additional noise sufficiently suppresses high-frequency oscillations in the data, enabling the algorithm to fit the long-wavelength trends. Such minima would be typically missed without additional nearby samples (models) in the parameter space; the user can then reconstrain the variable parameter limits near that minimum and restart the inversion algorithm. In general, inversion for any reflector may be possible when the standard deviation of the noise does not exceed the range of the time-shift variation.

The conclusions drawn for the P-wave time shifts for reflector C also apply to the S-wave shifts for reflectors A and B, which do not exceed 9 ms in magnitude (Figs. 2b and 4b). In contrast, the higher-magnitude S-wave time-shift curve for reflector C retains a distinct trend even after contamination with 10-ms noise (Fig. 5e), and the misfit surface possesses a well-defined global minimum (Fig. 5f).

Because time shifts of PS-waves above the reservoir are mostly controlled by P-wave lags, low-noise PS results for reflector A are similar to those for P-waves. The low-noise PS-wave shifts (Fig. 2c) from reflector B and those from reflector C with all noise levels give acceptable (albeit 3%–6% too low) estimations of ΔP (Fig. 4c).

Joint-misfit (P, S, and PS) inversions for all reflectors and noise levels produce accurate pressure values ($\pm 1.5\%$ of the reference ΔP). The best results using joint misfits are achieved at the reservoir top, with ΔP estimates for reflector C being somewhat inferior (Fig. 4d). However, joint misfits provide comparable or higher accuracy and improved consistency than each individual mode for the entire inversion set. This demonstrates the advantage of employing multiple wave types in pressure inversion.

Inverted reservoir length using P-, S-, and PS-waves (and their combination) from all reflectors is shown in Fig. 6. Due to the pronounced variations of time shifts beneath the reservoir with length, accurate inversion results for L (± 0.1 km of the actual value) are obtained for all wave types and noise levels at reflector C. As discussed above, P-wave time shifts at reflector A are masked by 5-ms noise and practically obliterated by 10-ms noise (Fig. 6a). Thus, similar to the inversion for ΔP, the seemingly accurate estimates of L for high-noise (10 ms) P- and PS-wave shifts for reflector A should be considered fortuitous. The P-wave time-shift magnitude increases near the reservoir top, and the length is well constrained by the P-wave reflections from interface B for all levels of noise. Optimal estimates of length from S- and PS-waves are obtained for reflectors B (except for data with $\sigma_{\text{noise}} = 10$ ms) and C. However, as with the pressure inversions, the combination of P-, S-, and PS-waves (joint misfits; see Fig. 6d) generally yields more accurate and consistent inversion results than each wave type alone.

Perturbations in the strain-sensitivity coefficients

There are few available measurements of the third-order stiffnesses C_{111} and C_{112} [see equation (3)]. Further, most published values correspond to dry core samples at room temperature subjected to a smaller strain compared with that of the reservoir. Also, stress applied in the laboratory typically is not triaxial. Hence, laboratory experiments cannot reproduce *in situ* conditions, and the third-order stiffness values will likely vary with temperature, saturation, and strain magnitude. Figure 7 displays inversion results obtained with the values of C_{111} and C_{112} perturbed by $\pm 20\%$. In agreement with the sensitivity study of Smith and Tsvankin (2013), a 20% increase in C_{111} causes a 15%–20% reduction in the inverted pressure (see the cluster on the left of the plot). The inverted ΔP for C_{111} reduced by 20% is approximately 15% higher. The perturbations of the coefficient C_{112}, whose magnitude is relatively small, have negligible influence on the inversion.

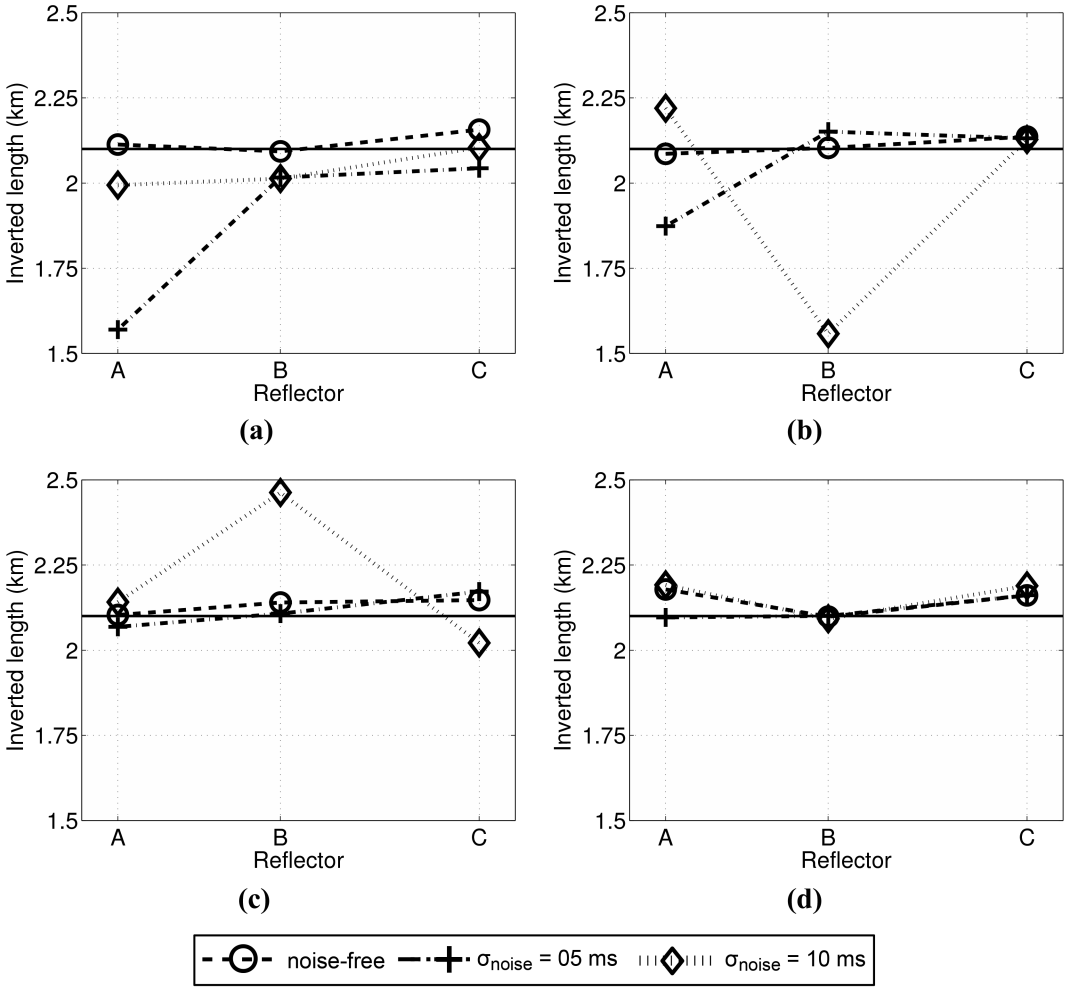

Figure 6 Reservoir length (L) estimated from time-shift misfits of (a) P-waves, (b) S-waves, (c) PS-waves, and (d) the combination of all three modes. The actual reservoir length (2.1 km) is marked by the solid line.

Figure 7 Inversion results obtained with distorted third-order stiffnesses values C_{111} and C_{112}. Each coefficient was perturbed by ±20%, as shown in the legend. The time shifts for the reference reservoir were obtained with the correct values of C_{111} and C_{112}. Inversions were performed using noise-free joint misfits [equation (5)] from each reflector (black markers: reflector A; blue markers: reflector B; and green markers: reflector C).

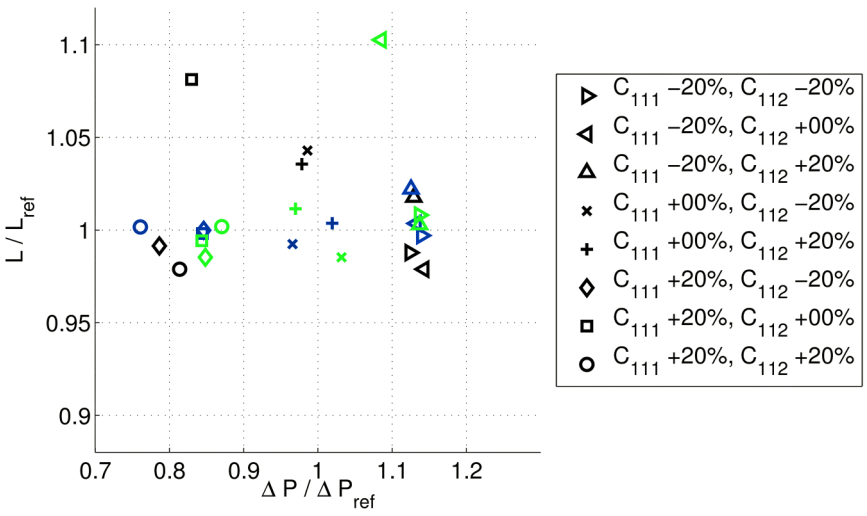

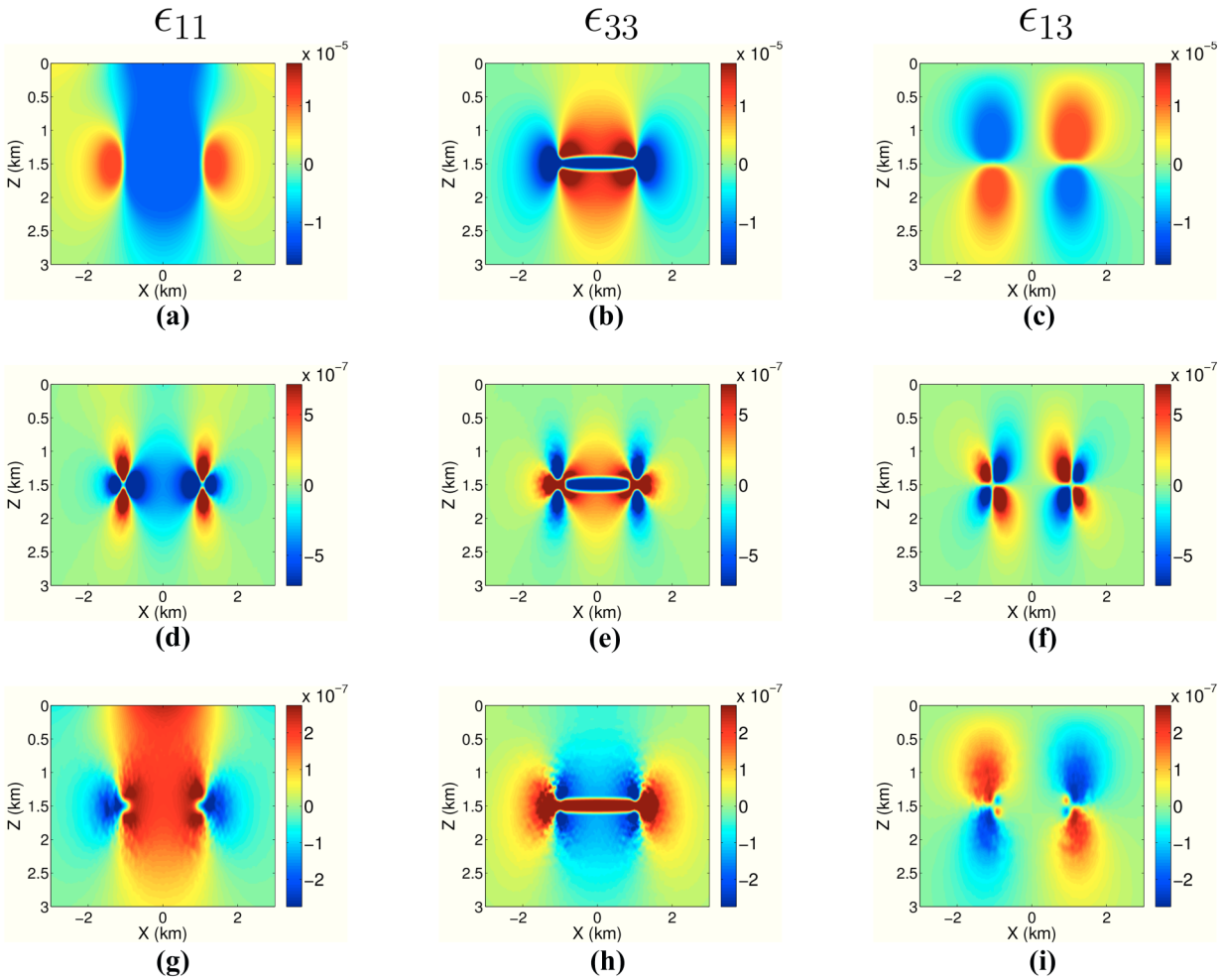

Figure 8 Comparison of the strain fields for the actual and inverted reservoir models. (a, d, g) The horizontal strain ϵ_{11}; (b, e, h) the vertical strain ϵ_{33}; and (c, f, i), the shear strain ϵ_{13}. The strains for the reference reservoir ($\Delta P = 17.5\%$, $L = 2.1$ km) are shown in the top row (a, b, c). The strain differences (i.e., the difference between the actual strain field and that for an inverted model) for the "best-case" S-wave and P-wave inversions are shown in the second (d, e, f) and third rows (g, h, i), respectively. Both best-case inversions were carried out for reflector C with 10-ms noise. The maximum percentage differences in the strain components for S-waves (d, e, f) are $\epsilon_{11} = 21\%$, $\epsilon_{33} = 4\%$, and $\epsilon_{13} = 11\%$, whereas those for P-waves (g, h, i) are $\epsilon_{11} = 3\%$, $\epsilon_{33} = 1\%$, and $\epsilon_{13} = 2\%$. The plots in each row have been uniformly scaled to the maximum standard deviation of the three fields in that row.

The estimated length is less sensitive to errors in C_{111} than is pressure, with almost all results for a 20% perturbation in C_{111} falling within ±5% of the actual value.

Accuracy in reconstructing the strain field

In Fig. 8, we illustrate the differences in the horizontal, vertical, and shear strains between the reference (actual) reservoir and the models corresponding to the best-case S- and P-wave inversions. In identifying the best inversion models, we consider only the results for noise-contaminated data. The strain fields have been smoothed to remove numerical singularities at the sharp corners of the reservoir, which helps reveal the nearby field structure where wells may be located or planned. Further, the plots in each row have been scaled to the maximum standard deviation of the strain component in that row. The actual maximum strain differences reach about 20%, with average strains for the inverted models deviating from the reference values by only 1%–2%.

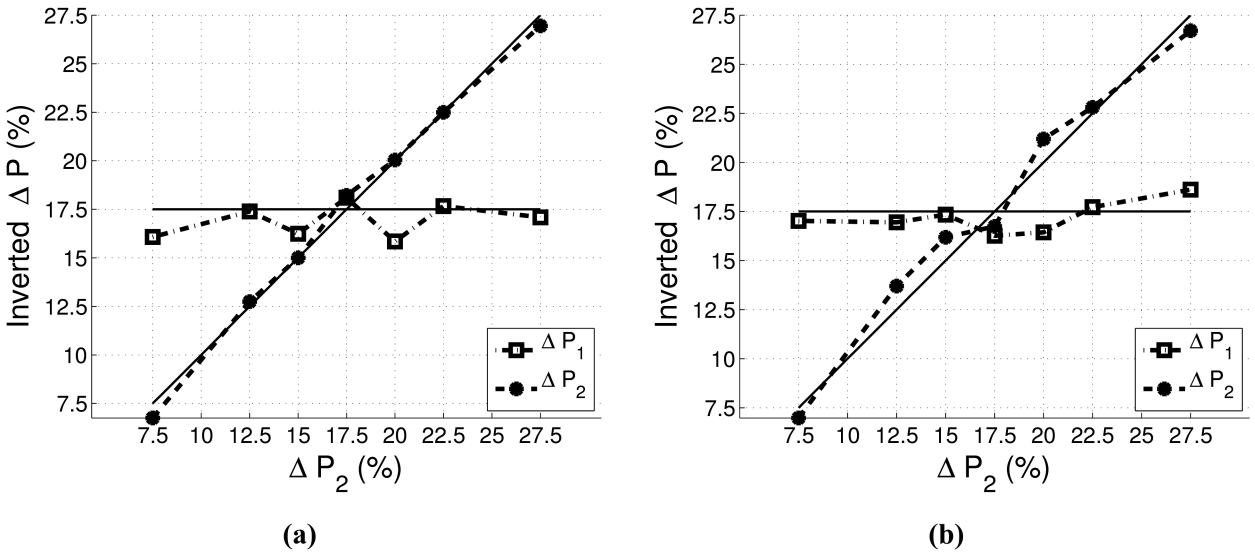

Figure 9 Best pressure-inversion results for the two-compartment reservoir model using input data with $\sigma_{\text{noise}} = 5$ ms. The pressure drop ΔP_1 in all tests is held at 17.5%, while ΔP_2 varies from 7.5% to 27.5% (actual values are marked by solid lines). The input data include (a) P-waves from reflector B and (b) S-waves from reflector C.

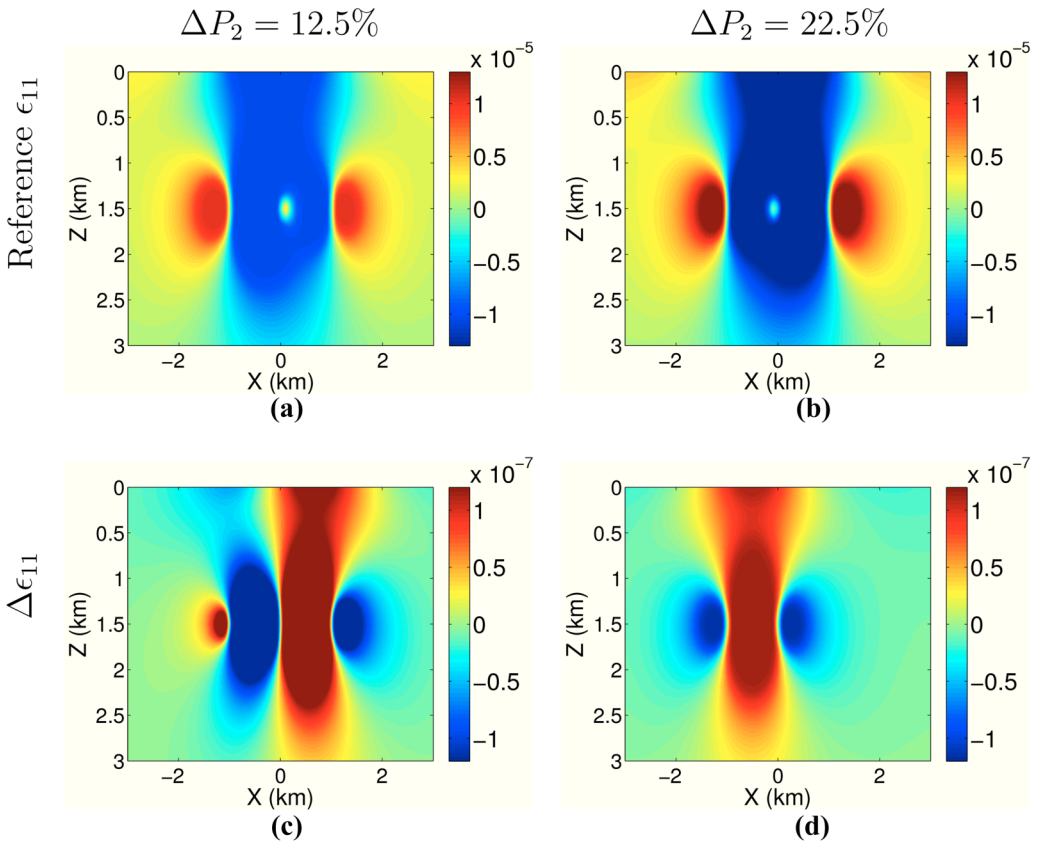

Figure 10 Fields of the horizontal strain ϵ_{11} for the two-compartment reservoir with $\Delta P_1 = 17.5\%$ and (a, c) $\Delta P_2 = 12.5\%$ and (b, d) $\Delta P_2 = 22.5\%$. (a, b) The actual (reference) strains. (c, d) The differences between the actual strains and those for the best-case P-wave inversion (using time shifts from reflector B with $\sigma_{\text{noise}} = 5$ ms).

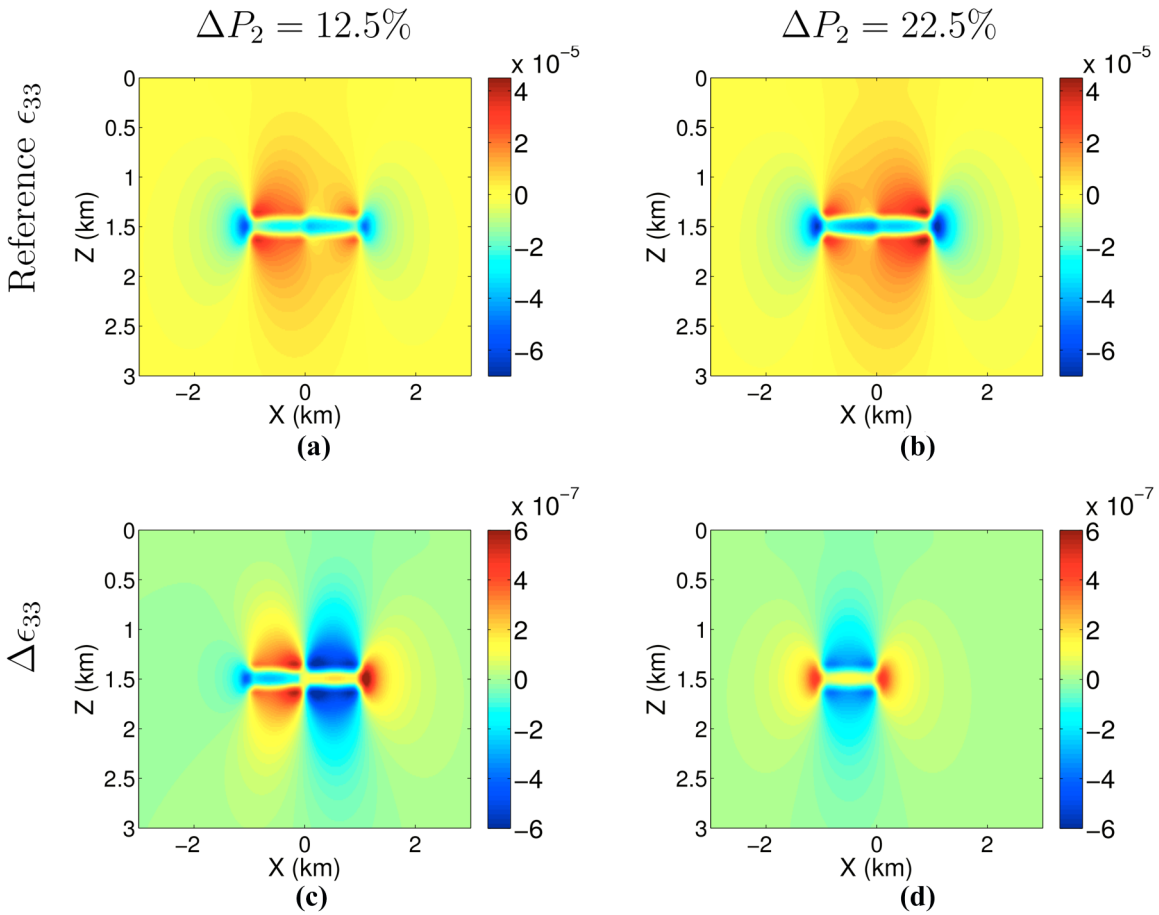

Figure 11 Fields of the vertical strain ϵ_{33} for the two-compartment reservoir with $\Delta P_1 = 17.5\%$; (a, c) $\Delta P_2 = 12.5\%$; (b, d) $\Delta P_2 = 22.5\%$. (a, b) The actual (reference) strains. (c, d) The differences between the actual strains and those for the best-case P-wave inversion (using time shifts from reflector B with $\sigma_{\text{noise}} = 5$ ms).

The model obtained from P-wave inversion (Fig. 8g, h, i) provides a better approximation for the strain field than that derived from S-waves (Fig. 8d, e, f). For both models, the largest vertical-strain differences are inside the reservoir and near the endcaps, whereas the most significant deviations in the horizontal and shear strains are observed at the endcaps. It should be emphasised that the best-case S- and P-wave models have close values of the pressure drop (differing by 2.5%). The errors in the estimated strains are confined to the vicinity of the reservoir, where the strain field is quite sensitive to small changes in reservoir pressure.

Pressure estimation for a two-compartment reservoir

The ability to resolve the pressure reductions of individual reservoir compartments is essential when the reservoir volume is separated by faults/seals or variations in porosity, permeability, or rock fabric that interfere with pressure communication.

To study which wave types and reflectors may be best suited for resolving multicompartment pressure differences, the reservoir in Fig. 1 is divided into two sections at $X = 0$, each measuring 1 km in length (the total reservoir length is assumed to be known as 2 km). The pressure drop ΔP_1 in one compartment is held at 17.5% (the value used in previous tests), whereas the pressure in the other compartment is varied within the range $\Delta P_2 = \Delta P_1 \pm 10\%$. Pressure variations inside the second compartment cause asymmetry in the time-shift curves (shown for a single compartment in Fig. 5a, b, c, e) with respect to the reservoir centre. As with the single-compartment pressure/length inversions, Gaussian noise ($\sigma_{\text{noise}} = 5$ ms and 10 ms) is added to the time shifts of the reference model. We simultaneously invert for the

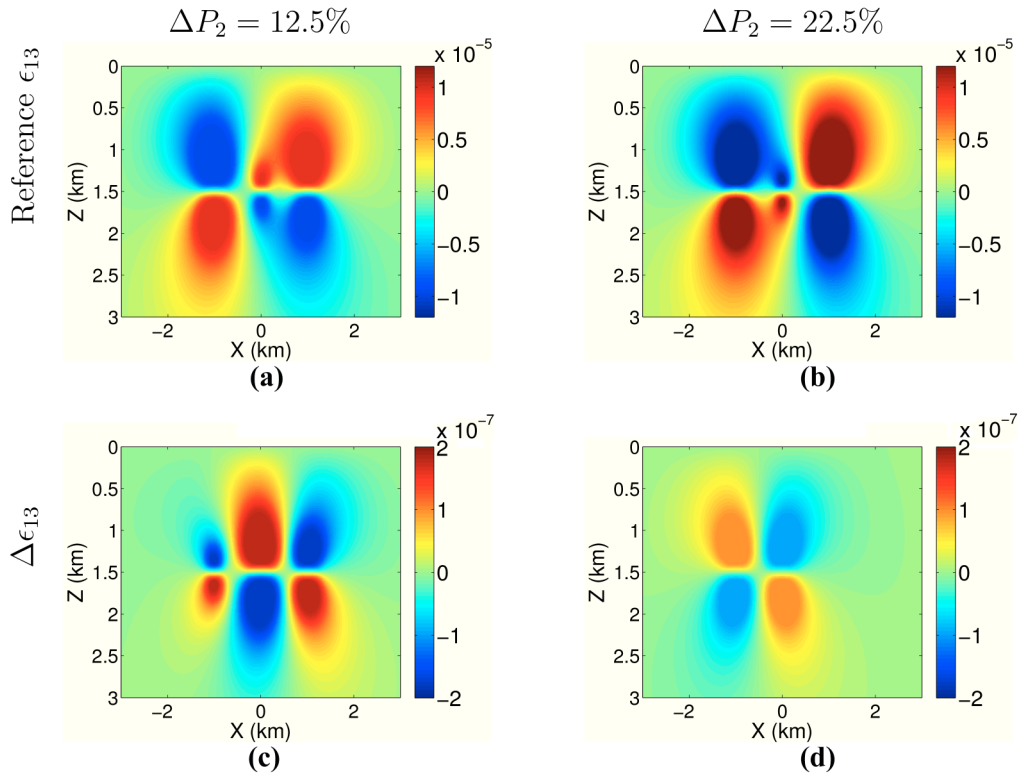

Figure 12 Fields of the shear strain ϵ_{13} for the two-compartment reservoir with $\Delta P_1 = 17.5\%$; (a, c) $\Delta P_2 = 12.5\%$ and (b, d) $\Delta P_2 = 22.5\%$. (a, b) The actual (reference) strains. (c, d) The differences between the actual strains and those for the best-case P-wave inversion (using time shifts from reflector B with $\sigma_{\text{noise}} = 5$ ms).

pressure drops in both compartments using a minimum of 40 and a maximum of 80 forward models.

Figure 9 shows two optimal pressure-inversion results obtained using P-wave time shifts from reflector B and S-wave shifts from reflector C, both with $\sigma_{\text{noise}} = 5$ ms. For the entire range of ΔP_2, both inverted pressure drops are within $\pm 2\%$ of the actual values. These errors are only marginally higher than those for the single-compartment pressure inversion discussed above (Fig. 4). Also note that the minimum number of forward models required to terminate the inversion is half of that for the single-compartment model. Similar results with slightly lower accuracy for ΔP_1 were obtained for the same wave types and reflectors with $\sigma_{\text{noise}} = 10$ ms. Therefore, P-wave time shifts from the reservoir top are sufficient for estimating the pressure differences inside the reservoir (i.e., S-wave data from reflector C are desirable but not necessary).

Similar to Fig. 8, Figs. 10–12 show the actual (reference) strain fields along with the errors in strain for the best inverted models corresponding to $\Delta P_2 = \Delta P_1 \pm 5\%$ (using P-wave time shifts from reflector B). The reference fields remain approximately symmetric laterally with respect to $X = 0$ for small deviations of ΔP_2 from ΔP_1. The strain asymmetry, however, becomes more pronounced with increasing difference between ΔP_1 and ΔP_2. The errors in the inverted strain components do not exceed 4%, which confirms the ability of our method to reconstruct excess strains in the entire section. Strain deviations are generally concentrated near the compartment with the smaller pressure drop, which is particularly evident from the lateral shift of the strain residuals in Figs. 10d, 11d, and 12d.

DISCUSSION

The results shown here may be considered optimistic compared with those that may be obtained by applying this method to field data. First, we use a known simple model geometry consisting of a single- or two-compartment reservoir with flat boundaries embedded in an initially homogeneous background, so the compaction produces well-understood stress and strain fields of relatively low complexity. Second, when generating seismic data and computing time shifts for

inversion, we have the ability to place strong reflectors at locations of our choosing. Consequently, we generate high-signal-to-noise reflections and clean time-shift data (except where arrivals interfere). Hence, the inverse problem discussed here is better conditioned than that for typical field sets, although we did study the influence of noise on the inversion results.

For example, when dealing with field seismic data, filtering of specific arrivals may be necessary for proper wavelet extraction. Amplitude variations with incidence angle or offset may occur with changing fluid saturation, so the ability to identify and isolate each wave type may differ. Thus, only sections of reflectors may be available for time-shift measurements. In this case, employing joint misfits [i.e., equation (5)] for combinations of suitable reflector segments and arrivals (P, S, and PS) may be necessary. Note that, while we have used only a single shot record for each reflector, improved results should be expected for multiple sources located both above and to the side of the reservoir.

The P-wave time shifts for our models are somewhat larger than those published in the literature for field time-lapse data (Rickett and Lumley 2001; Hatchell and Bourne 2005; Tura *et al.* 2005; Janssen *et al.* 2006; Hodgson *et al.* 2007; Rickett *et al.* 2007; Staples *et al.* 2007). Modifications to the modelling process such as adding a pressure-dependent effective stress coefficient α [equation (2)] will reduce changes in the stiffness values and thus the overall time-shift magnitudes (Fig. 2). Further, the strain-sensitivity coefficients used here (Sarkar, Bakulin, and Kranz 2003) were measured at room temperature on dry rocks under minimal strain. Hence, they are likely to be different from *in situ* values both inside and outside of the reservoir. Adjusting the geomechanical modelling to incorporate *in situ* reservoir rock physics may reduce the modelled strains and time shifts. However, the spatial patterns of time shifts around the reservoir (Fig. 2) will remain essentially the same, as will the time-shift variations with wave type. For example, the P-wave time-shift pattern in Fig. 2a is similar to the lower-magnitude time shifts measured for the Shearwater North Sea reservoir (Staples *et al.* 2007). Thus, the dependence of the inversion results on the input data and signal-to-noise ratio is adequately addressed by the presented study.

CONCLUSIONS

We have applied a hybrid global/gradient algorithm to evaluate the feasibility of inverting compaction-induced time shifts of P-, S-, and PS-waves for reservoir pressure and length. The time shifts were measured for three reflectors around single- and two-compartment reservoirs embedded in an initially homogeneous isotropic medium described by third-order (strain-sensitivity) stiffness coefficients. The hybrid inversion algorithm presented here extends the "nearest neighbour" method by estimating the local gradient at a subset of low-misfit models in the parameter space.

Our numerical analysis helps identify the reflector locations and wave types that should be used to invert for the reservoir parameters for different levels of noise. Reflectors in the overburden generate small time shifts that are suitable for inversion only when the data are essentially noise-free. The magnitude and lateral extent of time shifts increase near the reservoir, making it possible to invert even noisy P-wave reflections from the reservoir top for pressure changes. The most accurate pressure estimates for noise-contaminated S-and PS-wave data are obtained using reflections from interfaces beneath the reservoir, where the shear-wave time shifts reach their maximum values. Reservoir length is well constrained by the time shifts of all modes from the reservoir top (except for high-noise S and PS data) and from reflectors beneath the reservoir. Joint inversion of P-, S-, and PS-wave time shifts provides more accurate and consistent estimates of pressure and length than single-mode inversions for all three reflectors, demonstrating the benefits of acquiring and inverting multicomponent data.

It should also be noted that inversion of time shifts from deep interfaces typically requires computing fewer forward models. Inversion of joint (P, S, and PS) time shifts using models with $\pm 20\%$ errors in the strain-sensitivity coefficients resulted in comparable distortions in the pressure drop but insignificant errors in reservoir length.

For two-compartment reservoir models and moderate levels of reference time-shift noise, intercompartment pressure variations can be resolved with an accuracy of $\pm 2\%$ using P-wave time shifts from the reservoir top or S-wave time shifts from reflectors below the reservoir. The geomechanical model corresponding to the best-case P-wave inversion produces strain fields that differ by no more than 4% from the actual strains. These deviations are concentrated primarily around the compartment with the smaller pressure drop.

The results of this work can be used to model expected strain and stress changes around the depressurizing reservoir. The maximum differences between the strain values computed for the reference reservoir and the best inverted models are limited to about 20% of the reference strain.

ACKNOWLEDGEMENTS

The authors are grateful to Rodrigo Fuck (CWP, now Ion Geophysical), Mike Batzle (CSM/CRA), Roel Snieder (CWP), Jyoti Behura (CWP, now Seismic Science, LLC), Matt Reynolds (Applied Math, University of Colorado), and Ritu Sarker (CSM/CRA, now Shell) for discussions, comments, and suggestions, and to Jeff Godwin (CWP, now Transform Software) and John Stockwell (CWP) for technical assistance. The authors would like to thank the editor and reviewers of *Geophysical Prospecting* for helpful comments and suggestions. The paper by McCann and Wilts (1951) was made available via Stephanie Spika and the City of Long Beach Public Library. This work was supported by the Consortium Project on Seismic Inverse Methods for Complex Structures at CWP.

REFERENCES

Aster R.C., Borchers B. and Thurber C. 2005. *Parameter Estimation and Inverse Problems*. Academic Press.

Batzle M. and Han D. 2009. Rock and fluid properties: seismic rock physics. *SEG Continuing Education Series*, Denver Geophysical Society.

Calvert R. 2005. *Insights and Methods for 4D Reservoir Monitoring and Characterization*. Distinguished Instructor Short Course, Society of Exploration Geophysicists.

COMSOL AB 2008. COMSOL Multiphysics.

De Gennaro S., Onaisi A., Grandi A., Ben-Brahim L. and Neillo V. 2008. 4D reservoir geomechanics: a case study from the HP/HT reservoirs of the Elgin and Franklin fields. *First Break* **26**, 53–59.

Downs J. and Faux D.A. 1995. Calculation of strain distributions in multiple-quantum-well strained-layer structures. *Journal of Applied Physics* **77**, 2444–2447.

Fuck R.F., Bakulin A. and Tsvankin I. 2009. Theory of traveltime shifts around compacting reservoirs: 3D solutions for heterogeneous anisotropic media. *Geophysics* **74**, D25–D36.

Fuck R.F., Tsvankin I. and Bakulin A. 2011. Influence of background heterogeneity on traveltime shifts for compacting reservoirs. *Geophysical Prospecting* **59**, 78–89.

Geertsma J. 1973. Land subsidence above compacting oil and gas reservoirs. *Journal of Petroleum Technology* **SPE3730**, 734–744.

Greaves R.J. and Fulp T.J. 1987. Three-dimensional seismic monitoring of an enhanced oil recovery process. *Geophysics* **52**, 1175–1187.

Gubbins D. 2004. *Time Series Analysis and Inverse Theory for Geophysicists*. Cambridge University Press, London, UK.

Hatchell P. and Bourne S., 2005. Rocks under strain: strain-induced time-lapse time shifts are observed for depleting reservoirs. *The Leading Edge* **24**, 1222–1225.

Hearmon R. 1953. 'Third-Order' elastic coefficients. *Acta Crystallographica* **6**, 331–340.

Herwanger J. 2008. R we there yet? 70th EAGE annual international meeting, Expanded Abstracts, n. 4038.

Hodgson N., MacBeth C., Duranti L., Rickett J. and Nihei K. 2007. Inverting for reservoir pressure change using time-lapse time strain: application to Genesis field, Gulf of Mexico. *The Leading Edge* **26**, 649-652.

Hornby B.E. 1996. Experimental investigation of effective stress principles for sedimentary rocks. SEG Technical Program Expanded Abstracts, 1707–1710.

Hu S.M. 1989. Stress from a parallelepipedic thermal inclusion in a semispace. *Journal of Applied Physics* **66**, 2741–2743.

Janssen A.L., Smith B.A. and Byerley G.W. 2006. Measuring velocity sensitivity to production-induced strain at the Ekofisk field using time-lapse time-shifts and compaction logs. SEG Technical Program Expanded Abstracts, 3200–3204.

Landrø M. 2001. Discrimination between pressure and fluid saturation changes from time lapse data. *Geophysics* **66**, 836–844.

Lumley D. 2001. Time-lapse seismic reservoir monitoring. *Geophysics* **66**, 50–53.

MacBeth C. 2004. A classification for the pressure-sensitivity properties of a sandstone rock frame. *Geophysics* **69**, 497–510.

MacBeth C., Floricich M. and Soldo J. 2006. Going quantitative with 4D seismic analysis. *Geophysical Prospecting* **54**, 303–317.

Magnesan M., Depagne S., Nixon K., Regel B., Opich J., Rogers G. *et al.* 2005. Seismic processing for time-lapse study: Genesis field, Gulf of Mexico. *The Leading Edge* **24**, 364–373.

McCann G.D. and Wilts C.H. 1951. A mathematical analysis of the subsidence in the Long Beach-San Pedro area. California Institute of Technology.

Mindlin R.D. and Cheng D.H. 1950. Nuclei of strain in the semi-infinite solid. *Journal of Applied Physics* **21**, 926–930.

Rickett J., Duranti L., Hudson T., Regel B. and Hodgson N. 2007. 4D time strain and the seismic signature of geomechanical compaction at Genesis. *The Leading Edge* **26**, 644.

Rickett J. and Lumley D. 1998. A cross-equalization processing flow for off-the-shelf 4D seismic data. SEG Technical Program Expanded Abstracts **17**.

Rickett J. and Lumley D. 2001. Cross-equalization data processing for time-lapse seismic reservoir monitoring: a case study from the Gulf of Mexico. *Geophysics* **66**, 1015–1025, doi:10.1190/1.1487049.

Roste T. 2007. Monitoring overburden and reservoir changes from prestack time-lapse seismic data - applications to chalk fields. PhD thesis, Norwegian University of Science and Technology, Norway.

Sambridge M. 1999. Geophysical inversion with a neighbourhood algorithm - I. searching a parameter space. *Geophysical Journal International* **138**, 479–494.

Sarkar D., Bakulin A. and Kranz R.L. 2003. Anisotropic inversion of seismic data for stressed media: theory and a physical modeling study on Berea sandstone. *Geophysics* **68**, 690–704.

Sava P., Yan J. and Godwin J. 2010. SFEWE elastic finite difference wave-propagation development code for the Madagascar seismic software collection. *http://www.reproducability.org*.

Sayers C.M. 2010. *Geophysics Under Stress: Geomechanical Applications of Seismic and Borehole Acoustic Waves*. Distinguished Instructor Short Course, Society of Exploration Geophysicists, n. 13.

Sayers C.M. and Schutjens P.M. 2007. An introduction to reservoir geomechanics. *The Leading Edge* **26**, 597–601.

Schutjens P.M.T.M., Hanssen T.H., Hettema M.H.H., Merour J., de Bree P., Coremans J.W.A. *et al.* 2004. Compaction-induced porosity/permeability reduction in sandstone reservoirs: data and model for elasticity-dominated deformation. *SPE Reservoir Evaluation & Engineering* **SPE 88441**, 202–216.

Sen M.K. and Stoffa P.L. 1995. Global optimization methods in geophysical inversion. In: *Advances in Exploration Geophysics*, Vol. **4**. Elsevier Science.

Smith S. and Tsvankin I. 2012. Modeling and analysis of compaction-induced traveltime shifts for multicomponent seismic data. *Geophysics* **77**, T221–T237.

Smith S. and Tsvankin I. 2013. Sensitivity of compaction-induced multicomponent seismic time shifts to variations in reservoir properties. *Geophysics* **78**, T151–T163. doi: 10.1190/geo2012-0361.1

Staples R., Ita J., Burrel R. and Nash R. 2007. Monitoring pressure depletion and improving geomechanical models of the Shearwater field using 4D seismic. *The Leading Edge* **26**, 636–642.

Thurston R.N. and Brugger K. 1964. Third-order elastic constants and the velocity of small amplitude elastic waves in homogeneously stressed media. *Physical Review* **133**, A1604–A1610.

Tsvankin I. 2005. *Seismic Signatures and Analysis of Reflection Data in Anisotropic Media*, 2nd edn. Elsevier Science.

Tura A., Barker T., Cattermole P., Collins C., Davis J., Hatchell P., *et al.* 2005. Monitoring primary depletion reservoirs using amplitudes and time shifts from high-repeat surveys. *The Leading Edge* **24**, 1214–1221.

Wikel K.R. 2008. Three-dimensional geomechanical modeling of a tight gas reservoir, Rulison Field, Colorado. MS thesis, Colorado School of Mines, USA.

Yale D.P. and Jamieson W.H. 1994. Static and dynamic mechanical properties of carbonates. In: *Rock Mechanics, Models, and Measurements Challenges from Industry, Proceedings of the 1st North American Rock Mechanics Symposium* (eds P.P. Nelson and S.E. Laubach), pp. 463–471.

APPENDIX A

INVERSION ALGORITHM

Because time shifts are generally nonlinear in pressure (Smith and Tsvankin 2013), we have developed a hybrid inversion algorithm that combines the advantages of global and gradient methods. Gradient inversion algorithms (Gaussian, Levenberg–Marquardt, conjugate gradient, etc.; see Gubbins 2004; Aster, Borchers, and Thurber 2005) require the inversion to begin with a model close to the global minimum (true solution). However, the structure of the misfit function is unknown and may be complicated. Also, gradient algorithms typically need several forward models per iteration to compute the gradient (Jacobian) and curvature (Hessian) of the objective function, and estimate the update step size in the parameter space. Misfit data for all generated models typically are not retained for use in later iterations.

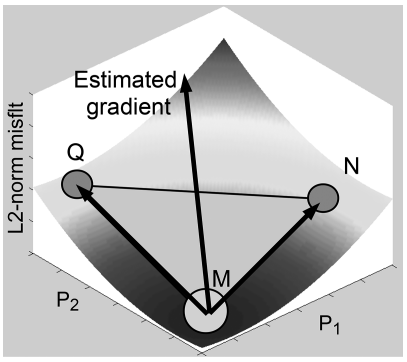

Figure A1 Local gradient estimation using nearest models in a 2D ($K = 2$) parameter space $[P_1, P_2]$. Each minimum-misfit model (point M) is assumed to be in a local minimum. The gradient direction is estimated by summing the vectors **MN** and **MQ**, where N and Q are the nearest models. If the misfits at N and Q are greater than that at M, new models are placed along and orthogonal to the estimated gradient vector at distances equal to $\pm(1/2)\min(|\mathbf{MN}|, |\mathbf{MQ}|)$.

The gradient portion of our algorithm is based on the "nearest neighbour" method of Sambridge (1999). The inversion begins with a regular distribution of initial models in the parameter space that have been randomly perturbed to assure that they are neither equidistant to each other nor to the centre of the parameter space (Fig. 3a). At each iteration, the algorithm computes the misfit for each forward model and selects a subset of minimum-misfit models to update. The nearest neighbour method divides the parameter space into Voronoi cells and updates minimum-misfit models using a Gibbs sampler or a random walk in each cell. In contrast, our algorithm estimates local gradients of the objective function in the region around the minimum-misfit subset and places updated models along the gradient direction.

Figure A1 illustrates the method used to estimate the local gradient for a subset of all current and previous models in the parameter space that possess the lowest misfits. Each model in this subset (point M in Fig. A1) is assumed to reside in a local minimum of the misfit surface. This assumption must be tested using the K-nearest models in the K-dimensional parameter space (points N and Q in Fig. A1 for our 2D space). If the K nearest models possess larger misfits, the direction of the gradient is estimated as the sum of the vectors between the minimum-misfit model and those neighbours. Model updates are inserted in the direction of the estimated gradient; one is located up-gradient, and one is located down-gradient. At least one additional model is added orthogonal to the gradient

should the current model reside at a saddle point. In the two-parameter inversions shown here, four update models were added at each iteration (two parallel and two orthogonal to the gradient) near the current misfit model. Each of these new models is inserted at one-half the distance to the nearest model used to estimate the gradient direction, which allows us to sample the local parameter space around each of the minimum-misfit models. Should none of the updated models possess a lower misfit, their data are simply incorporated into the gradient estimation at the next iteration. This results in a sequence of updates that converges downgradient toward the local minima (see Fig. A2a).

Note that computing Jacobians and Hessians is not required, and the method is computationally simple enough so that one can run many simultaneous gradient-tracking updates (i.e., gradient trackers). Further, this technique reduces convergence time compared with that of a standard global algorithm because models located in basins of convergence descend along the gradient in a systematic fashion (Fig. A2a; see also Appendix B).

Global inversion algorithms (Monte Carlo, Metropolis, genetic; see Sen and Stoffa 1995) can explore the entire parameter space and avoid local minima but typically require many more models than gradient techniques. Here, the goals are to sample parameter space efficiently to delineate the structure of the objective function and differentiate between local and global minima. In addition to the new "tracking" models placed up and down the estimated gradient, a user-defined number of "exploration" models are sequentially inserted into voids in the parameter space. These voids are identified by locations having the most common value of an N-dimensional potential function of the form $\sum_{i=1}^{N} 1/|\mathbf{r}|^{\gamma}$, where $|\mathbf{r}|$ is the distance between a prospective model location in the parameter space and the ith member of the current model set, and γ is a constant. If a smaller misfit value occurs at one of the exploration models, that model is incorporated into the subset of convergence/update models, and gradient estimation/tracking shifts to that region of the parameter space. Therefore, estimating and tracking the local gradient moves the search toward a local minimum, whereas the global/exploration models potentially make it possible to find the global minimum. As the inversion progresses, data from all computed forward models are saved in memory, which helps build the misfit surface by interpolation (Figs. A2a, b and 3). However, the complexity of the objective function (i.e., number of local minima) may dramatically increase for higher dimension parameter spaces. Further, visualization difficulties associated with a higher dimensionality of the parameter space can inhibit one's ability

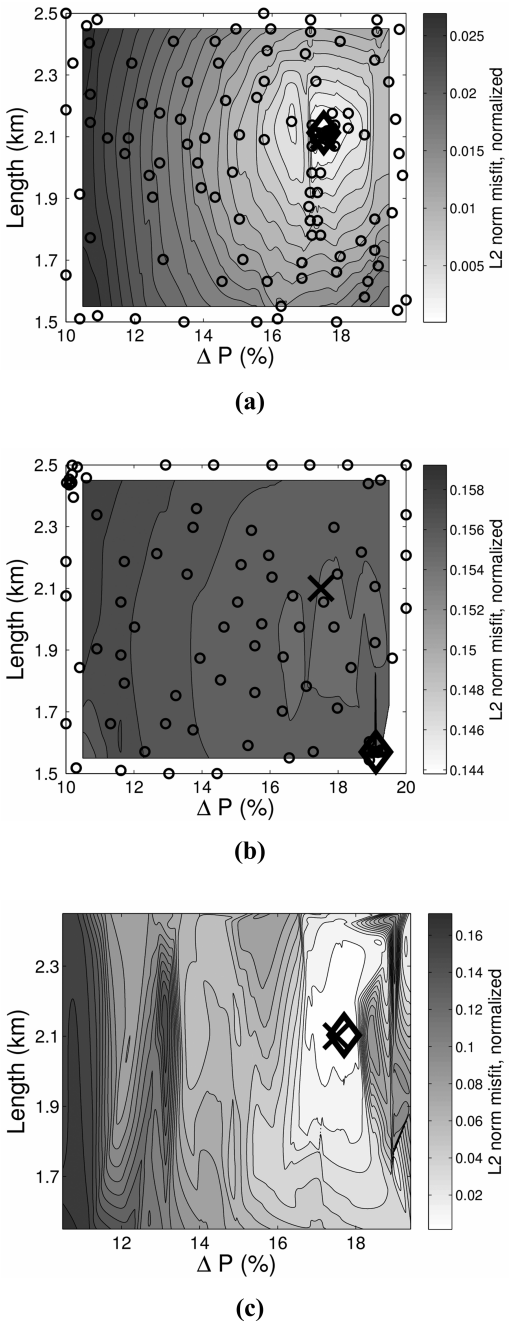

Figure A2 (a, b) Misfit (objective function) surfaces, for different levels of noise added to the reference reservoir time shifts. Black circles mark all forward models used in the inversion. The misfits are computed for P-wave time shifts from reflector A (a) without noise and (b) with $\sigma_{\text{noise}} = 5$ ms. The actual parameters are marked by crosses, whereas diamonds mark the final inversion results. (c) The misfit surface for the best-case PS-wave inversion (using noise-free shifts from reflector A). While this PS-result is accurate (cross and diamond overlap), the misfit surface is complicated enough to require the use of a global inversion algorithm.

to evaluate and reconstrain individual inversions (e.g., Sambridge 1999).

The inversion is typically terminated when changes in the user-specified misfit value fall below a specified tolerance level. It is necessary to specify a minimum and maximum number of iterations (or models) to be run before terminating the inversion. In some cases, the inversion halts when the total number of iterations or forward models passes a limit specified by the user. However, should the algorithm become trapped in one or more local minima, the user may increase the number of exploratory models per iteration, the number of gradient trackers, the minimum or maximum number of models to be run before termination, or all of these parameters.

In the examples shown here, the algorithm is implemented in a 2D parameter space, but the extension to higher-dimension parameter sets is straightforward. While not done here, interpolating the *N*-dimensional misfit surface may allow for an additional and potentially more accurate update model to be placed in the parameter space at the minimum of the interpolated misfit function. This provides an estimate of the global minimum, and placing a model there may increase the rate of convergence.

APPENDIX B

MISFIT SURFACES AND THE PERFORMANCE OF THE INVERSION ALGORITHM

The misfit curves for the full set of pressure and length inversions (Figs. 4 and 6) demonstrate "mixed-mode" behaviours that include smooth multistep reduction, large single-step drops, or both. The misfit curve in Fig. 3f is a representative example of this general behaviour. It is typical for the misfit to drop substantially in the first iteration when the misfit surface is simple and smooth. As the gradient-tracking part of the algorithm reduces the step size over iterations, misfit functions generate traditional "L-shaped" curves. However, the global portion of the algorithm may locate new local minima in the parameter space, or a gradient tracker may turn down a sharp slope. In this case, the misfit curve experiences a significant drop (e.g., between iterations 3 and 4 in Fig. 3f).

An example of the gradient-tracking behaviour of the algorithm is clearly seen in Fig. A2a where a series of models descends the misfit surface toward the actual $\Delta P = 17.5\%$. The misfit surface is interpolated using the entire set of inversion models (black circles) from the current and all prior iterations (no models are chosen/interpolated from the misfit surface). Note that the parameter space is well sampled by the global portion of the algorithm.

It is useful to study the misfit surfaces to gauge how well a multiparameter inversion is conditioned and determine whether or not the algorithm converges toward the global minimum. Fig. A2a shows a "bowl-shaped" misfit surface computed using noise-free P-wave time shifts from reflector A. The addition of noise to the time shifts for the reference reservoir not only increases the misfit magnitude but also smoothes the misfit surface by flattening the data's (time shifts) power spectrum. This reduces the complexity of the misfit surface (improves conditioning) and allows the gradient portion of the algorithm to perform more efficiently. However, as the noise level increases, coherent/desired data are masked and the misfit surfaces become over-smoothed (Fig. A2b). This flattens out local minima, creates an extended null space, and causes the inversion for noisy data from shallow reflectors to fail. In over-smoothed failed inversions, the minimum misfit is typically located away from the actual solution at the edges of the parameter space (diamond marker), as the global portion of the algorithm has not located any additional minima with a lower misfit.

A well-sampled parameter space with a complex misfit surface indicates poor conditioning, and the true solution cannot be found without employing the global portion of the algorithm. An example is given in Fig. A2c, which corresponds to the best inversion result for PS-waves. Although there is a well-defined basin of attraction, the misfit surface is generally complicated, and there is the potential for multiple local minima. This requires a global algorithm to locate the neighbourhood of the actual model for this particular problem and parameter space.